Simulation of Wing and Nacelle Stall

Rolf Radespiel[1], Daniela Gisele François[2], David Hoppmann[3], Simon Klein[3], Peter Scholz[4]
Institute of Fluid Mechanics, Technische Universität Braunschweig, Hermann-Blenk-Str. 37, 38108 Braunschweig, Germany

Katharina Wawrzinek[2], Thorsten Lutz[4]
Institute of Aerodynamics and Gas Dynamics, Universität Stuttgart, Pfaffenwaldring 21, 70569 Stuttgart, Germany

Torsten Auerswald[2], Jens Bange[5]
Environmental Physics, Eberhard Karls Universtät Tübingen, Hölderlinstr. 12, 72074 Tübingen, Germany

Christoph Knigge[6], Siegfried Raasch[5],
Institute of Meteorology and Climatology, Leibniz Universität Hannover, Herrenhäuser Str. 2, 30419 Hannover, Germany

Simon Übelacker[2], Rainer Hain[6], Christian J. Kähler[7],
Institute of Fluid Mechanics and Aerodynamics, Universität der Bundeswehr München, Werner-Heisenberg-Weg 39, 85577 Neubiberg, Germany

Philip Kelleners[6], Ralf Heinrich[8]
Institute of Aerodynamics and Flow Technology, DLR, Lilienthalplatz 7, 38108 Braunschweig, Germany

Silvia Reuß[2], Axel Probst[6], Tobias Knopp[6]
Institute of Aerodynamics and Flow Technology, DLR, Bunsenstr. 11, 37073 Göttingen, Germany

Numerical stall simulations are challenging in terms of physical models involved, overall computation effort, and the needed efforts for validation. The present paper describes coordinated, fundamental research into new simulation methodologies and their validation for wing and nacelle stall that also include the effects of atmospheric gusts. The research was carried out by the DFG funded Research Unit FOR 1066, which is composed of German Universities and the German Aerospace Center, DLR. The Research Unit investigated advanced models of turbulence, advanced physics-based gust models, and new numerical approaches for gust simulation. These modeling and computational activities are supplemented by new validation experiments, that aim at providing stall data on wings and engine nacelles with well defined, generic distortions of the onset flow.

I. Introduction

THE prediction of stall behaviors at low speed is an important part in the design of commercial transport aircraft. Take-off and landing performance is generally a strong driver of aerodynamic design. The ability to predict

[1] Professor and Head of Institute, AIAA Associate Fellow
[2] Research Assistant
[3] Research Assistant, AIAA Member
[4] Senior Research Scientist and Head of Research Group, AIAA Member
[5] Professor and Head of Research Group
[6] Senior Research Scientist
[7] Professor and Head of Institute
[8] Senior Research Scientist and Head of Research Group

maximum lift and the associated angle of attack along with all force and moment coefficients within aerodynamic design cycles can accelerate industrial design processes and avoid costly design changes later on.

Aircraft design regulations require careful verification of maneuverability and the assessment of aircraft loads over the complete operational range. This involves the quantification of gust effects within the aircraft design process. Moreover, current practice for defining the operational margins to stalling speeds at climb and approach are also based on the current knowledge of gusts encountered during these flight phases. The research hypothesis followed with the present work is that improved characterization of gusts and improved capabilities in the simulation of interactions between maximum lift and gust will eventually improve flight safety and allow for better exploitation of aircraft take-off and landing performances.

The German DFG Research Unit 1066[1] addresses three fundamental research areas of aerodynamic stall effects. These are the simulation of aircraft wing stall, the simulation of aircraft nacelle stall and the assessment of engine fan stability for inhomogeneous inflow. The present contribution reviews first two research areas while the last one is covered in a separate paper[2].

The research approach of DFG Research Unit 1066 involves a coordinated effort in the area of physical modeling of turbulent flows, in advanced numerical simulation methods and in experimental validation. The area of physical flow modeling not only covers the high Reynolds number flows of aircraft wings but also the modeling of atmospheric disturbances. Hence, five university institutes and the German Aerospace Centre, DLR, contribute to the work presented here. Technische Universität Braunschweig contributes an advanced Reynolds stress model (RSM) of turbulence. As wing stall usually involves complex 3D boundary layers, juncture flows and the effects of longitudinal vortices we assume that RSM will eventually result in satisfactory capture of all these flow features. The research on the RSM addresses also the question whether hybridization of RSM and local DES can improve the prediction of strong flow separations. Leibniz Universität Hannover and Universität Tübingen provide advanced models for atmospheric distortions. Here, two approaches are followed: Universität Tübingen contributes a statistical model of atmospheric turbulence that is based on flight data of a sophisticated probe located well below a helicopter in low level flight. Leibniz Universität Hannover, on the other hand, uses high-resolution Large Eddy Simulations of the convective atmospheric boundary layer to extract and characterize gust samples as well as supplying 3D atmospheric flow fields. These atmospheric disturbance models are input to aerodynamic wing simulations with the flow solver TAU of the German Aerospace Center, DLR. With the TAU code, atmospheric disturbances can be simulated by using moving Chimera grids. These Cartesian grids carry the disturbances from the wing far field to the wing proximity. The Chimera approach allows taking all aerodynamic interactions of atmospheric disturbances and the wing flow field into account. Additional research work by DLR implements and investigates a range of gust interaction models that aim for improved computational efficiency.

The complex simulation approaches of the present work require validation, in particular as we address atmospheric free stream distortions where the smallest resolved length scale is in the order of the wing chord. Therefore, Technische Universität Braunschweig provides a wind tunnel experiment by which controlled disturbances are generated upstream of a high-lift airfoil, while a similar experiment of nacelle stall with controlled distortions is performed by Universität der Bundeswehr München.. These experiments are representations of generic 2D gust interactions. Three groups at Universität Stuttgart, Technische Universität Braunschweig and the DLR in Göttingen use these experimental configurations to perform numerical rebuilding of the wind tunnel tests.

Initial research results of the Research Unit 1066 were already presented two years ago[3]. The present paper reviews the progress that this group has made until the project end in July 2015.

II. Turbulence Modelling for Stall Simulations

A. RANS model

The aerodynamics of wings at stall usually involves a broad range of flow scales. While the unsteady behaviors of separating turbulent boundary layers go along with vortex shedding and flow hysteresis a consistent turbulence model for these flows is not known. Moreover, for aircraft flows with Reynolds numbers around 10^7 and above there is no real alternative to using RANS models of turbulence for the global flow field. We note that aircraft flows at high lift coefficients are generally much affected by vortical flow in junctures and longitudinal vortices that stem from flap edges, nacelle strakes, pylons or from other desired or unavoidable geometric discontinuities. Moreover, stall is usually affected by anisotropy of normal stresses, non-alignments of stress and strain, and non-equilibrium of turbulence production and dissipation. Our philosophy is that Reynolds-stress models of turbulence (RSM) can represent these effects in a suited way to predict the onset of flow separation with sufficient accuracy.

The aerodynamic flow simulations of the DFG Research Unit 1066 use the DLR TAU code[4]. The turbulent Reynolds stresses are computed with the JHh-v2[5] and JHh-v3[6] Reynolds stress models which are extensions of the

Jakirlić-Hanjalić homogeneous (JHh) RSM[7]. The six Reynolds-stress equations are modeled using a linear redistribution term Φ_{ij} and a generalized-gradient model for turbulent diffusion. An algebraic anisotropy model computes the homogeneous dissipation-rate tensor ε^h_{ij} from the scalar value ε^h that describes the homogeneous part of dissipation. In this model low-Reynolds-number damping functions in the stress redistribution model and the ε^h-equation are calibrated with the aid of DNS data. This allows for accurate representation of the near-wall stress and dissipation anisotropies. The transport equation for ε^h of the JHh-v2 model[5] is extended by additional non-equilibrium terms that describe the effects of pressure gradient and rapid changes of turbulent length scale. This model was calibrated for a range of subsonic and transonic flows. More recently, the model was further extended to better represent separated flows with strongly curved velocity profiles. This extension was named JHh-v3 model[6]. It is based on the hypothesis that the second velocity derivative augments the turbulent length scale.

For consistent simulations of laminar-turbulent transition, a novel approach using extended linear-stability-based modeling was developed within the DFG Research Unit 1066[8]. Here, in addition to an e^N-method for transition prediction, the contributions of the 2D Tollmien-Schlichting waves to the statistical Reynolds stresses are computed and inserted in the RANS solution at the computed transition location. Thus, turbulence onset is initiated in a physically sound way. As shown in Ref.8 this ensures unique transition and separation behavior, whereas conventional point-transition modeling may yield unphysical laminar flow.

While the long-term strategy of turbulence representation is based on RSM, a number of computations use the well established Menter SST two-equation model of turbulence[9].

B. Hybrid RANS/LES model

It is now widely accepted that local Large Eddy Simulations present an efficient way to resolve the dynamic behavior of large separated flow areas. One approach for seamless combination of RANS modeling in attached boundary layers with local LES in separated regions is the detached eddy simulation (DES). To apply the JHh-v2 RSM in a DES, the (homogeneous) dissipation-rate tensor is scaled by the ratio of the RANS length scale to the hybrid length scale of the respective DES-model. The hybrid length scale is here provided by the algebraic delayed DES approach (ADDES)[10]. It uses the basic definition of delayed DES (DDES) for the hybrid length scale, l_{hyb}:

$$l_{hyb} = l_{RANS} - f_d \cdot \max\left(0, l_{RANS} - C_{DES} \cdot \Delta\right),$$

but replaces the delay function, f_d , by a combination of algebraic boundary-layer criteria. These are evaluated along wall-normal lines. Attached boundary layers are shielded from so-called modeled-stress depletion by estimating the boundary-layer edge using the δ_{99} criterion, whereas separation locations are estimated via a critical value for the boundary-layer shape factor H_{12}. This approach succeeds in detecting pressure induced separations at smooth aerodynamic surfaces that are usually not recognized by the common DES sensors. Thus, the RANS modeling (f_d = 0) can be explicitly used in attached regions and the interface to LES (f_d = 1) is placed at the separation point. C_{DES} is a model constant calibrated as C_{DES} = 1.1 for JHh-based DES to make them act similar to a conventional subgrid-scale LES model. Moreover, a low-Reynolds number correction is applied in the LES region in order to avoid excessive damping of the sub-grid stresses. More details are found in Ref. 11.

A major problem of current research is the occurrence of the so called "grey zone", where the fluid passes from the RANS region to the local LES regions. In this transition zone, the modeled Reynolds stresses diminish by the hybrid length scale formulation but the resolved turbulent fluctuations have not yet grown to their physical levels. A crucial ingredient of a suited hybrid scheme is hence to force the generation of turbulent content in the LES branch, within the separated flow region. Two models were investigated by the Research Unit: In the stochastic SGS model the Reynolds stresses are multiplied with random numbers with an expectation value of one. These numbers are recomputed at each node and in each physical time step. The second, alternative model is to provide synthetic turbulence (ST) at the inflow to the local LES region. The strategy is to extract stress levels and turbulent length scales from the close-by RANS region and use that information to inject physics-based fluctuations into the LES region.

The newly developed ST model is based on concepts of Ref. 12. The algorithm was further improved to attain a low artificial flow divergence of the generated velocity field of fluctuations and to model their advection through the domain where fluctuations are added. The generated velocity field is inserted into the flow field through a source term in the governing flow equations[13]. The source terms are activated in a volume domain right after the RANS/LES interface by algebraic sensors, following the ADDES-procedure of above. The model reads

$$\vec{u}'(\vec{r},t) = \boldsymbol{A} \cdot \sqrt{\boldsymbol{6}} \cdot \sum_{n=1}^{N} \sqrt{q^n} \cdot \vec{\sigma}^n \cdot \cos\left(k^n \cdot \vec{d}^n \cdot \vec{r}' + \Phi^n + S^n \frac{t'}{\tau}\right).$$

Here, the tensor A is obtained by Cholesky decomposition of the Reynolds stress tensor provided by the RANS solution upstream of the RANS/LES interface ($R=A^TA$) to ensure that the generated forcing velocity field reproduces the anisotropy and non-homogeneity of the upstream modeled boundary layer. The inlet reference position $\vec{r}'$ and the auxiliary time t' define advection of the generated velocity field in the streamwise direction. The inlet reference position, $\vec{r}'$, is obtained by a streamline approximation procedure that links each point of the forced domain to a reference point at its inlet[14]. The auxiliary time, t', is the time when the currently computed fluctuation has gone through the inlet reference position, $t' = t - |\vec{r} - \vec{r}'|/U_{conv}$, where the convective velocity, $U_{conv,}$ is defined as 0.6 times the boundary layer edge velocity. The implementation of this forced convection based on Taylor's hypothesis significantly reduces the required distance to achieve fully developed turbulence[15]. Additionally, the unit direction vector $\vec{d}^n$ is perpendicular to $A_{ref} \cdot \vec{\sigma}^n$, where A_{ref} is the tensor A defined at suitable reference location. With this condition, the divergence of the generated velocity field is largely reduced[14].

The fast development of resolved turbulent structures is supported by a modified filter width in the LES formulation, given by

$$\Delta_\omega = \sqrt{\frac{1}{2}\sum_{j\in F_i} \vec{N}\cdot\vec{n}_{ij}} \quad \text{, with} \quad \vec{N} = \frac{1}{|\vec{\omega}|}\,\vec{\omega} \quad \text{, and} \quad \vec{\omega} = \frac{1}{2}\left(\frac{\partial u_i}{\partial x_j} - \frac{\partial u_j}{\partial x_i}\right) \quad ,$$

where F_i denotes the set of neighbors of the control volume V_i and $\vec{n}_{ij}$ is the area-weighted face normal vector between the control volumes V_i and V_j. Additionally, the artificial dissipation in the skew-symmetric energy preserving central discretization scheme is optimized for scale-resolving simulations according to Ref. 16.

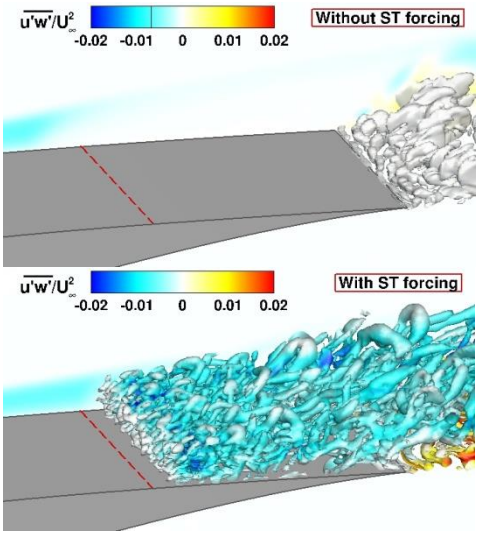

Figure 1. Contours of the Q-criterion colored by resolved shear stresses. The background plane shows modeled shear stress. The dashed red line depicts the RANS/LES interface location

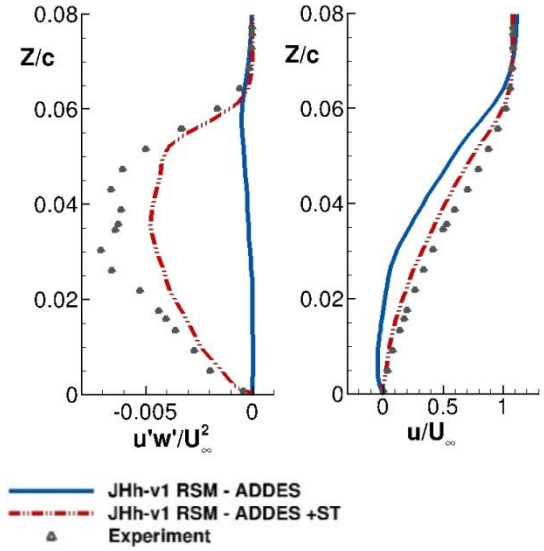

Figure 2. Reynolds shear stress (left) and mean streamwise velocity (right) profiles at x/c = 0.90 of the upper surface of the HGR-01 airfoil

The synthetic turbulence forcing was assessed by simulating airfoil stall and stall of a flow-through nacelle. The here used HGR-01 airfoil is represented with a grid of 7.6×10^6 points which were carefully refined in the near-trailing-edge area to satisfy the local LES requirements. The computation was performed at freestream conditions given by M=0.076, $Re=0.65\times10^6$, and the angle of attack, α=12deg. The non-dimensional time step was $0.5x10^{-3}$. Fig. 1 shows the resolved turbulence near the trailing edge area of the HGR-01 airfoil computed with and without synthetic turbulence forcing. It can be seen, that without applying synthetic turbulence forcing only minor turbulent structures with negligible shear stress appear. In contrast, well-defined, three-dimensional turbulent structures develop downstream the RANS/LES interface when the synthetic turbulence forcing is applied, resulting in a smooth and almost continuous transition from modeled and resolved shear stresses. This is also be observed in Fig. 2 where the shear stress profile obtained with synthetic turbulence forcing fairly matches the experimental data, while the computation without forcing generates no significant turbulence above the airfoil surface. The implementation of the

synthetic turbulence also improves the computation of the mean flow (Fig. 2, right) and consequently the separation size and mean pressure coefficient distribution (Fig. 3).

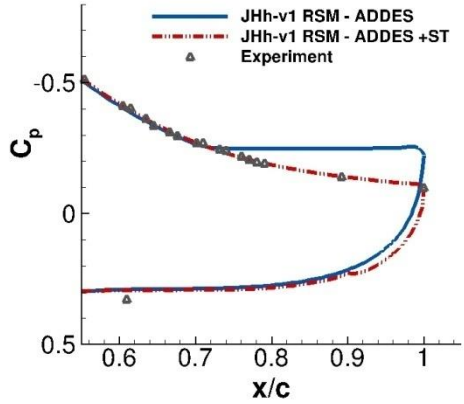

Figure 3. Mean pressure coefficient distribution near trailing edge area of the HGR-01 airfoil

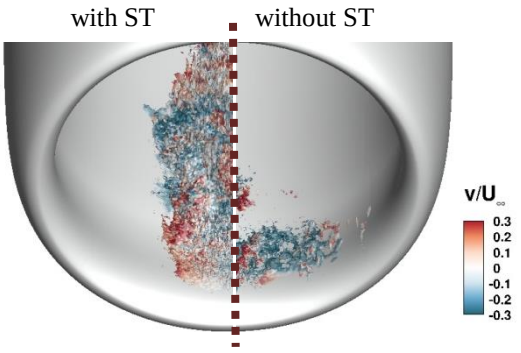

Figure 4. Iso-surface of $u/U_\infty = 0$

The nacelle grid consists of around 10×10^6 points distributed to resolve flow separation at the lower inlet contour at large angles of attack[17]. The chosen computational point is Ma=0.15, Re=1.32×10^6, α= 25deg. The non-dimensional time step was $0.63\text{x}10^{-3}$. It turns out that the numerical results obtained with ST forcing slightly overestimate the separation size with respect to experiments at the given angle, Ref. 31 (not shown here), while the numerical results obtained without ST forcing strongly underestimate the separation size. Fig. 4 contrasts the separation sizes obtained with and without ST forcing. Fig. 5 compares the shear stresses at the symmetry plane of the nacelle provided by PIV and the ones obtained by the numerical simulation with ST forcing. For a suited comparison, results at slightly different angles of attack are compared that exhibit similar separation size (PIV: α = 25.5deg; computation: α = 25deg). The numerical results slightly underestimate the shear stress. This lack of resolved shear stresses might be due to grid resolution.

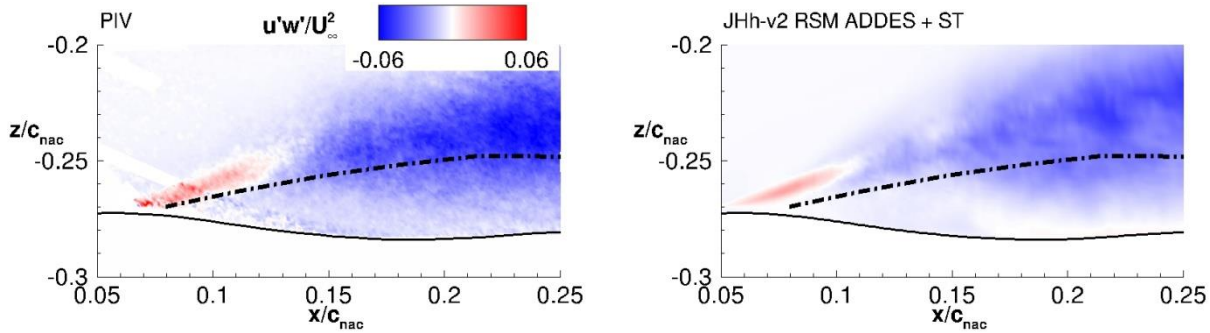

Figure 5. Reynolds shear stress in the symmetry plane of the nacelle. Left: experiments[17], right: computation with synthetic turbulence forcing

PIV data revealed that vortex-type structures are generated at the separation onset and move downstream through the outer part of the separation area (Fig. 6a). Corresponding field snapshots were also extracted from the numerical simulations (Fig. 6b,c). The results with ST forcing show rather good agreement for the general velocity field of fluctuations, the development of the vortex structures, and the trajectory of the structures, revealing a similar dynamics. Whereas the flow solution without ST forcing indicates a separated flow without quasi-periodical generation of vortex structures.

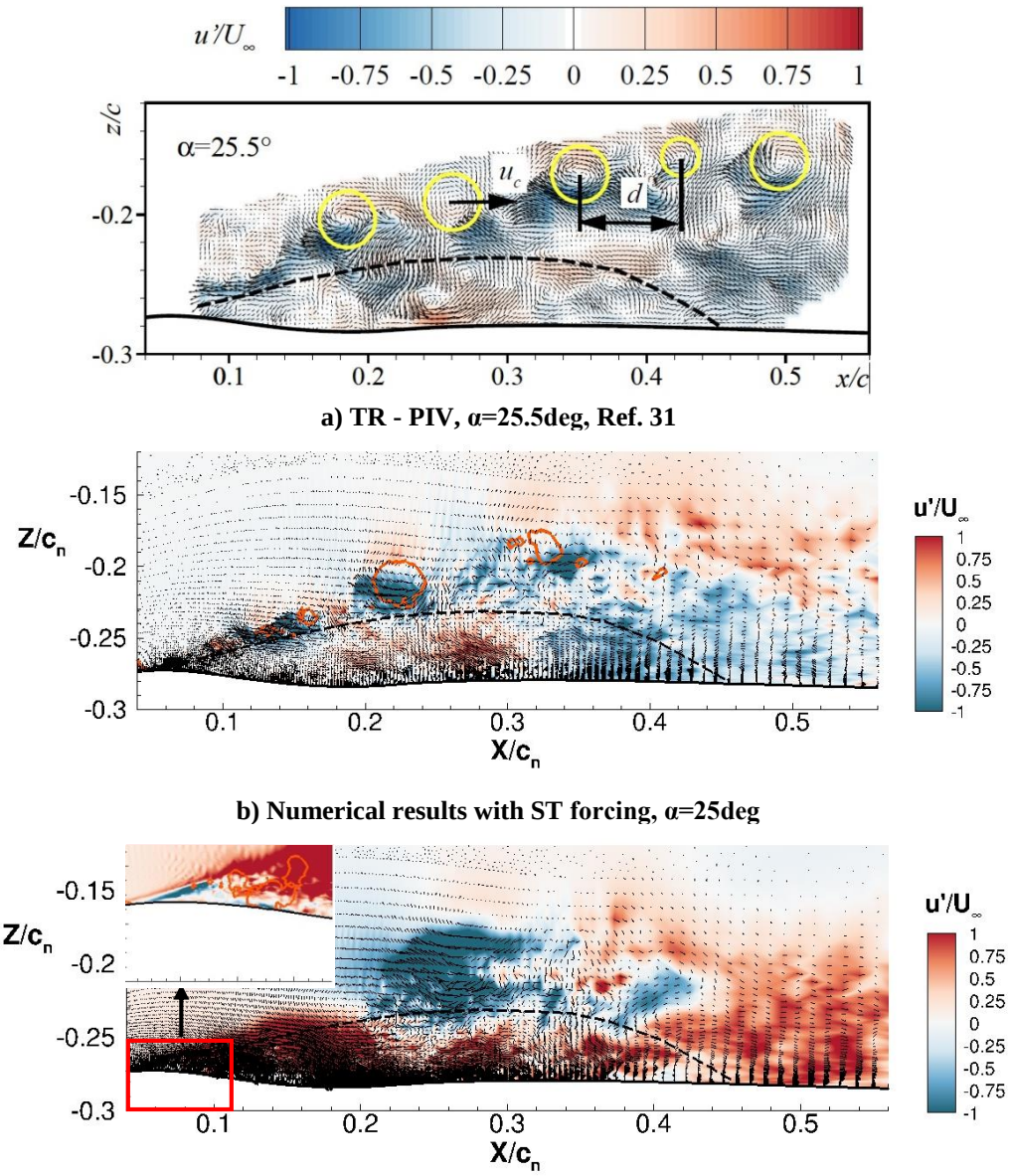

Figure 6. Instantaneous vector field of the velocity fluctuations in the symmetry plane of the nacelle. The orange lines in b) and c) enclose low density areas exposing vortex core locations.

III. Gust Modeling and Simulation of Local Atmospheric Environments

Modern numerical simulation methods and advanced in-flight measurements provide the opportunity to obtain a physics based characterization of the atmospheric boundary layer with its strong, discrete wind pulses also known as gusts. The well-known (1-cos)-law which is described in the Federal Aviation Regulations for Transport can thus be scrutinized and improved. Furthermore, LES data of the atmospheric boundary layer enable analysis of the two-dimensional structure of the wind gusts. This is an improvement over the previous approaches where measurements only provided one-dimensional data.

The atmospheric LES solver PALM used for the present work has been developed at the Institute of Meteorology and Climatology at the Leibniz Universität Hannover[18]. PALM solves the filtered non-hydrostatic, incompressible Boussinesq equations, the first law of the thermodynamics and the equation for turbulent kinetic energy (TKE). It

scales very well on parallel computers and hence, it enables simulations with a resolution down to 1-2 meters. PALM furthermore allows to simulate the turbulent wind field for large cities[19] or, as in the present study, around single buildings.

A relevant meteorological scenario causing intensive turbulence is a stormy low-pressure system that has been used to scrutinize relevant gust shapes. To obtain the information about discrete gusts from the time-depending three-dimensional data output of the simulation, horizontal cross sections at different heights are extracted. Several one-dimensional virtual measurements in these instantaneous flow fields provide statistical, space depended information of the velocity components. The results show that the one-dimensional mean gust shapes are more complex than the simple (1-cos)-law suggests[20]. Mean gust shapes obtained from LES tend to be broader, with a rather constant middle part and a steeper variation towards the gust edge. Gust shapes also vary with the gust length. Smaller gusts are more similar to the (1-cos)-shape whereas the longer gusts are steeper. The LES database allows for analyzing two-dimensional gust shapes also. Therefore, all gust shapes exhibit an ellipsoidal character. The eccentricity increases from smaller to longer gusts. Along the major axis the longer gusts have a middle part with low variation, comparable to the results of one-dimensional gust shapes. Analysis of gust shapes was performed for different flight altitudes (10 m - 500 m)[20]. These two-dimensional characterizations have not done before and might be important for future maneuverability assessment of transport aircraft.

An alternate approach for atmospheric flow field characterization is based on in-flight measurements. Data are measured using an airborne measurement probe attached to a helicopter. Measurements are taken at various flight altitudes as well. Several sensors (e.g. wind vector, temperature, humidity) sampled at 100 Hz are mounted for high-resolution measurements in the atmospheric boundary layer. A large data set of measurements for different meteorological scenarios is available including atmospheric flow in various thermal stratifications (stable, very stable, neutral, convective). As basis for the generation of the turbulent wind field from this in-flight data the Fourier approach is used, in which the sum is taken over several waves with different wave numbers to build a random velocity field. The resulting wind field is divergence-free and isotropic. By applying the Cholesky decomposition, the wind field can be modified to possess a predefined correlation matrix which introduces anisotropy.

A cross validation of the synthetic turbulence field with PALM data was also performed. For this purpose PALM simulation results were used to extract generic flight data along virtual flight paths. These data were then used to create the synthetic wind field. While the given statistics are reproduced very well, some features like coherent structures cannot be generated[21].

Further PALM simulations were devoted to analyzing atmospheric distortions at airport runways as a result of large buildings. Previous simulations of Nieuwpoort et al.[22] guided the shape of the obstacle. Fig. 7 displays a schematic view of the building, the runway, and the wind conditions can. The undisturbed upstream flow was purely shear driven. The neutrally stratified boundary layer reached a height of 1500 m, where a geostrophic wind of 20 m/s was predefined. Red and blue arrows indicate the corner streams with high wind speed values as well as the low wind speeds downstream of the building in Fig. 7. The touchdown zone of the virtual runway is outside the building wake, so that the building-induced turbulence affects the landing aircraft during the final approach at an altitude of several decameters.

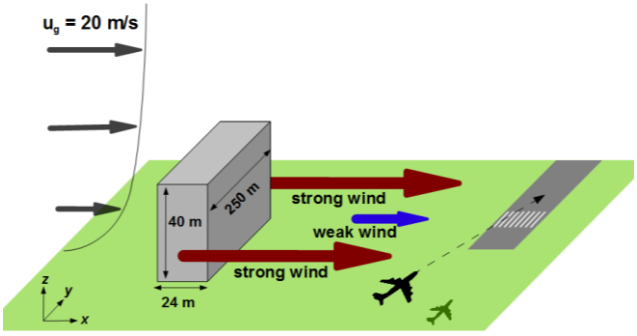

Figure 7. Schematic view of the simulated flight path through the wake of the building

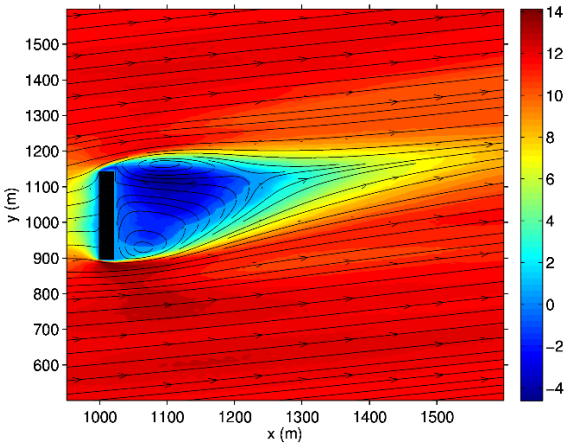

Figure 8. Mean flow around the building (black rectangle) in a horizontal cross-section in the middle of the building height at z= 20 m. The mean u-component (crosswind) in m/s is colored.

For a brief overview of the flow around the building, a horizontal cross-section of the mean airstream is shown in Fig. 8. The mean crosswind (colored) was calculated by averaging the wind speed component u over a time period of 60 min. Additionally, streamlines with arrows indicate the direction of the flow. The typical recirculation zone behind the obstacle is marked by the two horizontal vortices. At the right end of the recirculation zone, the stagnation point occurs approximately 200 m behind the trailing edge of the building. Most of the smaller scaled turbulent eddies (not visible in Fig. 8) are generated between the large vortices of the mean flow and the corner streams (flow around the corners of the obstacle) where high velocity gradients occur. The slight asymmetry of the flow which is visible in the horizontal cross-section is a result of the slight rotation of mean wind direction in the boundary layer due to the Coriolis force.

The distance between the obstacle and the virtual runway (or virtual flight path) is 450 m. The assumed flight path is parallel to the y-axis and has an angle of 5°. Along the runway, starting from the touch down point, an altitude of 10 m above ground was defined to extract the wind speed data. Results of the data extraction along the flight path are shown in Fig. 9. Virtual flights were performed in both mean and instantaneous flow conditions. The temporal development of the turbulence was considered by assuming an airspeed of 70 m/s. Thus, the complete flight duration is about 16 s along the 1100-meters-long flight path. The wind speed measurements in Fig. 9 can be divided into three periods which differ considerably from each other: Firstly, the region before the building wake (flight path = 500 m – 1000 m) has mean wind speeds of more than 13 m/s and turbulent fluctuations of about 1-2 m/s. Secondly, the region of the wake (1000 m – 1300 m) with strong turbulent perturbations exhibits a reduction of the mean wind of more than 5 m/s. Thirdly, the region behind the wake (1300 m – 1600 m) where the aircraft reaches the ground (at flight path = 1400 m and z = 10 m) is different again. In this third region, the close ground surface causes lower mean wind speeds of approximately 10 m/s - 11 m/s but stronger fluctuations (up to 5 m/s) than in the first region. In contrast to the typical turbulent fluctuations of a shear driven atmospheric boundary layer in the first and third region, the building induced fluctuations in the second region reach more than 10 m/s. A closer look to the maximum differences between the turbulent crosswind speeds along the flight path reveals that they reach 15.5 m/s and 13.6 m/s over a distance of about 150 m - 200 m. The mean wind deficit, in contrast, is 6.1 m/s and 3.6 m/s, respectively. We note that all the wind speed differences marked in Fig. 9 meet the 7 knots (3.6 m/s) criterion (both in mean and instantaneous velocities). Following this criterion, the perturbed area may have a significant influence on the maneuverability of a landing aircraft.

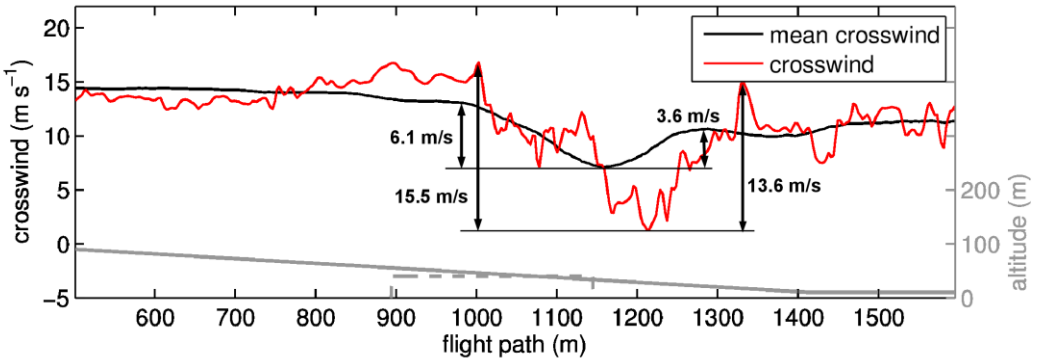

Figure 9. Virtual mean and instantaneous crosswind measurements along the flight path. The building and the flight path are indicated as gray lines.

IV. Simulation Approaches for Wing Stall including Gusts Effects

The prediction of unsteady loads caused by atmospheric effects like gusts is essential for aircraft development. Gust loads are important for the design of the structure but also for the layout of the control surfaces and the flight control system. With respect to maximum loads, especially gusts of high amplitude and wave-length being long relative to the reference chord length are of interest. But also gusts of shorter wave-length can be of relevance, if the aircraft flys close to maximum lift. In that case gusts of short wave-length can trigger wing-stall. In the DFG Research Unit 1066 methods for the prediction of the unsteady behavior for both situations (short and long wave-length) are developed, based on the DLR TAU-Code.

One method for modeling of gusts is the so called Disturbance Velocity Approach (DVA)[23]. This is rather easy to implement in CFD codes and allows the usage of standard meshes for aerodynamic analysis. The method captures the

influence of the gust on the aircraft but it does not model the feedback of the aerodynamics of the aircraft on the gust shape. Therefore, for gusts of short wavelength a certain prediction error can be expected. Hence an alternate approach was also implemented in TAU: The gust is fed into the discretized flow field using an unsteady boundary condition at the farfield. The advantage of the so call Resolved Gust Approach (RGA) is that the mutual interaction of gust and aircraft is captured. However, a high resolution in the whole domain is required, in order to accurately advect the gust from the inflow boundary to the aircraft. To compare these methods, a generic 2D test case representing a wing and horizontal tail plane (HTP) is used. The grid, as used here, is an overset mesh. Component meshes for wing and HTP are placed into a Cartesian background mesh. An additional grid with a high resolution in flow direction is used for the advection of the gust from the farfield boundary to the wing-HTP configuration. The number of points used for the individual meshes is the result of careful grid sensitivity studies. Computations have been made for 3 different gust wavelengths (1, 2 and 4 wing chord-lengths). As gust shape the classical (1-cos)-law has been selected. Two different on-flow Mach numbers are used, to allow for assessing the influence of compressibility. For the Mach number of M=0.25, we expect nearly incompressible flow, whereas compressibility effects can be expected for M=0.75. The gust amplitude is 10% of the on-flow velocity. The angle of attack α is 0 deg. Since the airfoils of wing and HTP are symmetrical, the resulting lift is purely created by gust loading.

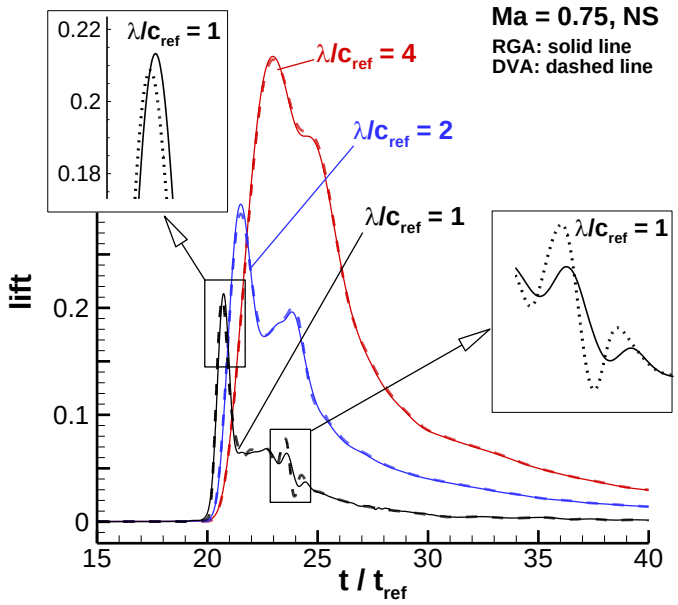

Figure 10. Comparison of lift versus dimensionless time predicted by DVA and RG approaches

$$err_{C_{L,\max}} = \frac{\left|C_{L,\max,RG} - C_{L,\max,DVA}\right|}{\left|C_{L,\max,RG}\right|}$$

	$err_{C_{L,\max}}$ [%]	
$\underline{\lambda}=\lambda / c_{ref}$	*Ma = 0.25*	*Ma = 0.75*
1	*2.16*	*11.08*
2	*1.24*	*2.93*
4	*0.47*	*0.64*

Table 1. Maximum lift prediction error of DVA approach

Figure 10 shows the comparison of results of the DVA (dashed lines) and the more accurate RGA (solid line) for the transonic test case. The lift history computed for all three wavelengths is plotted versus dimensionless time. Time is made dimensionless using the time t_{ref} of a gust needed to travel a distance of one reference chord length c_{ref} with velocity u_{inf}. The agreement of the simple approach with the accurate approach predicting the mutual interaction is surprisingly good. Almost no difference is visible for the wavelength of 4 and 2 chord lengths for *Ma=0.25*. The error of the DVA for prediction of the maximum lift is only *0.47%* for $\underline{\lambda} = \lambda / c_{ref} = 4$ and *1.24%* for $\underline{\lambda} = 2$. The situation is similar for *Ma=0.75*, but compared to nearly incompressible flow the prediction error is higher (*2.93%* for maximum lift for $\underline{\lambda} = 2$). A larger difference is visible for the short wavelength of one chord length for the dimensionless time between 23 and 25, corresponding to the time when gust and HTP interact. The peaks are over-predicted by the DVA, since this method does not capture the effect of the wing aerodynamic on the gust shape. Additionally, the maximum lift found with the DVA is under-predicted for Ma= 0.75, see also the zoom-in in Fig. 10. The error of 11.08% for transonic flow is significant. For the incompressible regime the error is still below 2.5%, which is acceptable. A similar study, as described above, has also been made for a full 3D configuration with similar results[24].

Apart from the generic gust encounters studied above, examples of disturbed oncoming flow are flights through atmospheric turbulence, wakes from large buildings during takeoff or landing at crosswind conditions and strong confined trailing vortices from preceding (larger) aircraft. Studying these flow examples in detail with a RANS-method requires the simulation method to both resolve and advect the coherent fluid structures over large physical

distance. As demonstrated in the previous investigation, a CFD-method of second-order accuracy, as typically used for aircraft performance computation, requires a high-density mesh throughout all of the domain and as such may suffer from high computational expense when used as a simulation tool. Presently designated higher-order methods, that are of spatial order higher than two, are better suited to resolve and evolve fluid structures without unphysical dissipative losses, on grids of moderate density. This could lower the computational cost. However these higher-order methods may not be well suited to simulate flows with discontinuities like strong shocks in transonic flow, or thin boundary layers close to complex shaped solid structures embedded in the fluid. The solution adopted here is a zonal approach. Within this zonal approach, the flow domain of interest is simulated with different discretization methods each being applied in those regions where their strengths excel. In the implementation of this zonal approach the boundaries of the different grids overlap and the developing flow state is coupled in these overlapping regions. This procedure is called the Chimera or overset grid approach, and the overlapping grids are also referred to as Chimera grids, see Chesshire[25]. For a more elaborate treatment of the solution procedure and illustration in detail with an example the reader is referred to Kelleners[26].

In the zonal approach presented here the aircraft geometry and its near field is simulated with the hybrid-grid DLR TAU-code. The domain from near field to far field, discretized on Cartesian grids, is simulated with a higher-order adaptation, see Enk[27], of the structured multi block DLR FLOWer-code. Compact finite difference schemes, or Pade schemes, as published by Lele[28], are used for discretization of the spatial terms for either the Euler or the Navier-Stokes equations of fluid flow. The current implementation of the Pade scheme is of fourth order accuracy.

Two test cases demonstrating the accuracy and potential of this simulation method are presented here: airfoil-gust interaction and airfoil flight through LES-simulated atmospheric turbulence. In the first case, (1-cos)-shaped gusts of wave lengths of one, two and four airfoil chord lengths are allowed to advect through the higher-order Cartesian domain and then interact with a NACA0012 airfoil at a Mach number of 0.5. The general layout of the far field mesh block topology with a gust of wavelength four moving towards the airfoil in the center of the domain is given in Fig. 11.

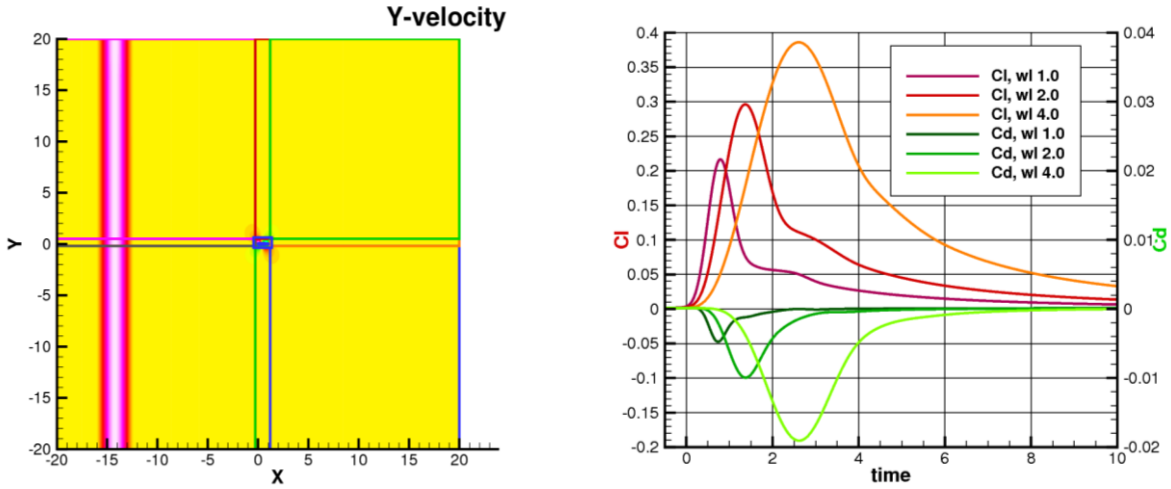

Figure 11. Computation domain for the airfoil-gust interaction test case (left) and variations of lift and drag cefficients of NACA 0012 airfoil during gust-airfoil interaction for three different gust wave lengths, wl (right)

Fig. 11 also displays lift and drag coefficients evolving in non-dimensional time for the gust-airfoil interaction, for the gust wavelengths of one, two and four chord lengths. The negative drag coefficient indicates that for these flow conditions the airfoil experiences thrust similar to flapping wings of birds. The accurate results verify the validity of the zonal approach and represent a further support for the usefulness of the previous DVA-method for simulation of gusts with large wavelengths.

In the previous cases of gust interaction, the disturbances of the atmosphere were modeled with a one-dimensional analytic function. Although this is standard practice for analyzing gust response, higher fidelity models simulating disturbed flow fields in multiple dimensions are needed as well. Inflow and advection of atmospheric turbulence computed with the LES model PALM[18], allows for simulation of airfoil interaction with atmospheric turbulence of greater realism. The pre-computed turbulent flow field of the present application results from assuming a constant geostrophical wind of 10 meters per second above a purely shear-driven boundary layer with an altitude of 700 meters.

The PALM simulation was run until statistical quantities for the turbulent flow field indicated that a quasi-steady turbulent state was reached. The snapshot of the flow field in Fig. 12 shows the variation of the iso-Mach lines as NACA0012 moves through the turbulent atmosphere at Ma=0.33 and at one degree of angle of attack. The turbulent flow field enters at the left boundary, passes over airfoil at the center of the domain and leaves through the outflow boundary where a sponge layer boundary condition prevents reflection of spurious waves. Variations of the lift and drag coefficients with time are given in Fig. 13. The initially almost constant values for the airfoil lift and drag coefficients result from the time needed for the turbulent atmospheric phenomena to travel from the inflow boundary towards the airfoil. The relative variations of the lift coefficient of up to 25 percent during the further course of simulation indicate a considerable influence of the turbulent flow field on the airfoil for these flow conditions. The new capability to resolve realistic gust ensembles with zonal aerodynamic computations offers new insight into the physics of aerodynamic interactions as well as the potential to reduce uncertainty margins associated with idealized gust models.

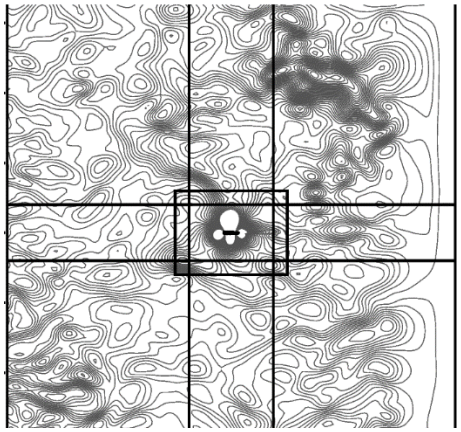

Figure 12. Snapshot of the unsteady flow field, presented as iso-lines of the Mach number

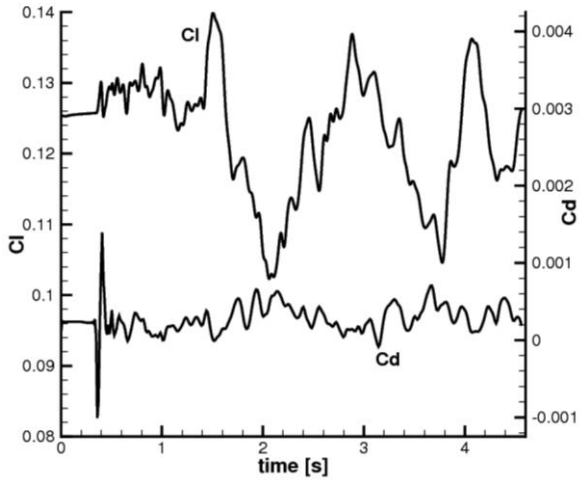

Figure 13. Variation of lift and drag coefficients with time for flight of NACA 0012 airfoil through turbulent atmosphere.

V. Validation

The Research Unit conducted a series of new validation experiments in two different wind tunnels. These experiments aimed at studying the effects of short-wave-length gusts on airfoil and nacelle stall. The gust is represented by a transversal vortex that moves with the onset flow to the wind tunnel model. The free vortex is generated by a symmetrical, two-dimensional NACA 0021 airfoil (vortex generator airfoil) mounted upstream of the wind tunnel model at which stall experiments are to be conducted. As the vortex generator airfoil changes its angle of attack and its circulation, a layer of vorticity is created in the vortex generator wake. Crucial for the properties of the vortical disturbance is the pitching rate, which determines the spatial extent of the created disturbance while the pitching amplitude determines the strength of the wake vortex. The current set up obtains 10deg pitch amplitude at a rate of 0.7deg/ms which creates a wake structure with a length in the order of the high-lift airfoil chord length. This motion is obtained by using a light-weight vortex generator airfoil along with a fast actuation pitching unit, based on digital linear actuation. Four linear servo actuators are arranged in pairs, one pair to the right and one to the left side of the vortex generator airfoil as shown in Fig. 14. For operating several actuators in parallel, synchronization is provided by a master-slave control system. Details of the fast-actuation pitching system as well as the properties of the generated vortical disturbance are given in Ref. 29 .

A. Experiments on a Flow Through Nacelle

The objective of this experiment was to characterize the effect of small, generic gusts on the internal flow of the nacelle[30]. The flow-through nacelle is axis-symmetric. It has a chord length of c_n = 526 mm and a highlight diameter of 315.6 mm. Since the experiments were performed at a relatively low mass flow rate and at a low onflow Mach number, M=0.11, the shape of the inner side of the nacelle was modified in a way that would achieve a pressure induced separation[31]. The experiments were conducted in the Eiffel-type atmospheric wind tunnel of the Universität der Bundeswehr München with a closed, rectangular test section. The inflow velocities during the experiments were adjusted to obtain $Re_c \approx 1.25 \cdot 10^6$.

Figure 14. Motion apparatus used for the vortex generator airfoil

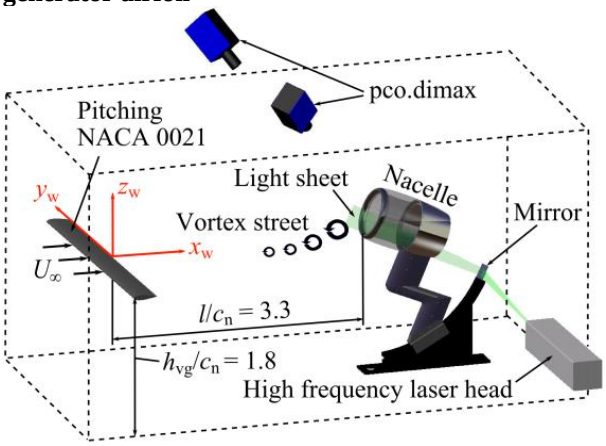

Figure 15. Experimental Setup: The trailing edge of the airfoil is placed 3.3 dimensionless length units upstream of the lower lip of the nacelle.

The vortex generator described above was used to generate generic gusts in the wind tunnel, see Fig. 15. The trailing edge of the airfoil was positioned at 3.3 normalized length units upstream and on the same height as the lower leading edge lip of the nacelle. Therefore, a strong effect of the vortex street on the internal nacelle flow is obtained. We note, that due to the curvature of the streamlines caused by the lift of the nacelle, the vortices are advected through the nacelle. Fig. 16 (a) shows the pitch history of the airfoil. It pitched from α_{vg} = -11deg to α_{vg} = 11deg within Δt_{norm} = 4.1, paused at α_{vg} = 11deg for Δt_{norm} = 13.9, pitched back to α_{vg} = -11deg within Δt_{norm} = 5.6, and paused again at α_{vg} = -11deg for approximately 11.9 normalized time units. The normalized time is given by $t_{norm} = t \cdot U_\infty / c_n$. The plot shows that one cycle lasts 35.6 normalized time units. Due to the gradual change in the angle of attack of the symmetric airfoil from α_{vg} = -11deg to α_{vg} = 11deg, a shear layer develops, which then rolls up and multiple single vortices develop and move downstream. The clockwise rotating vortex street is visualized with the d_2-criterion and plotted with the virtual contour of the nacelle in grey in Fig. 16 (b). This criterion separates vortices from shear - and boundary layers[32]. The freestream velocity was subtracted from the mean phase-locked vector field and the roll up of the shear layer occurs due to the Kelvin-Helmholtz-Instability. The shift of the vortices in the z_w-direction comes from the pitch of the airfoil around the 1/3 chord of the airfoil, which leads to a downward movement of the trailing edge of the airfoil. Note that the shift to the upper right corner of the most downstream advected vortices is likely increased by the induced velocity of the vortices on their neighboring vortices, as the single vortices are all rotating counter clockwise. This counter clockwise rotating vortex street is considered to be critical due to the fact that it increases the temporal angle of attack of the nacelle.

Static pressure measurements were conducted in order to find the angle of attack with separation onset. It became apparent that separation occurs between $\alpha_n \approx$ 20deg and $\alpha_n \approx$ 21deg at steady, undisturbed inflow conditions with the airfoil at a steady angle of attack of $\alpha_{vg} \approx$ -11deg. Moreover, time resolved, stereoscopic Particle Image Velocimetry (SPIV) and Kulite® experiments were performed in order to characterize the effect of the vortex street on the flow through the nacelle. The time resolved SPIV System is shown in Fig. 15. The light sheet was positioned in the front lower part of the symmetry plane of the nacelle. Furthermore, tufts were used to confirm that the flow was symmetrical in its mean. The trigger signal was set when the vortex generator passed α_{vg} = -10deg, see Fig. 16 (a). The measurement was then started shortly later and 30 - 105 images were acquired. This cycle was repeated 1000 times. Therefore, 1000 phase-locked vector fields were averaged for given times after the trigger signal. The presented results are for an angle of attack of α_n = 21deg.

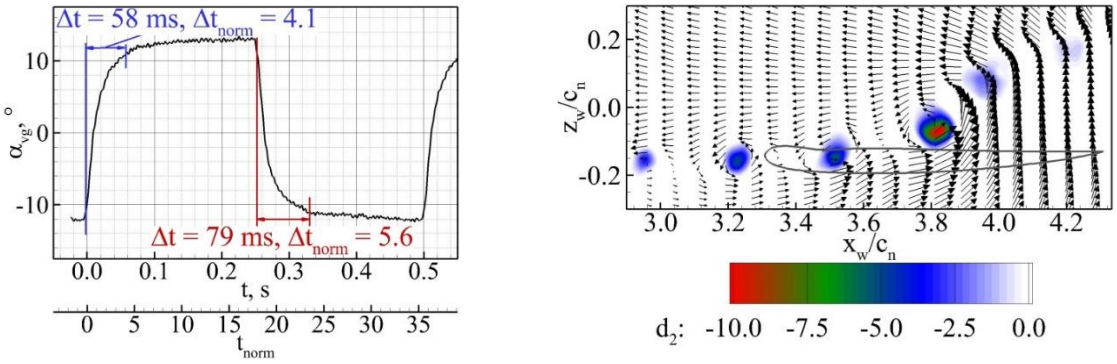

Figure 16. Vortex generator. Angle of attack of the pitching airfoil (left) and vector field with subtracted freestream velocity in the dynamic wake of the airfoil without the nacelle in the test section. Vortices are visualized with the d_2-criterion[4] (right).

In the upper part of Fig. 17, the *x*-component of the velocity *u* is shown in the symmetry plane of the nacelle, whereas in the lower part, the normalized turbulent kinetic energy is plotted. While Figures (a) display the result for the normalized time $t_{norm} = 2.3$, Figures (b) illustrate the vector field for the time $t_{norm} = 4.0$ after the trigger signal. The black lines in the upper Fig. 17 are iso-lines of the streamwise velocity in the coordinate system fixed to the nacelle. The *x*-axis points downstream, parallel to the nacelle's axis of symmetry, while the *z*-axis points upward and *y* in the spanwise direction. The normalized time 2.3 displays the steady undistorted flow, whereas $t_{norm} = 4.0$ shows the flow in the nacelle when the impact of the distortion is at its maximum. At this instant, the separation and the corresponding low speed area is significantly bigger. To conclude, the generated vortex street disturbs the steady phase-locked flow field in the inlet significantly. While the present separation bubble at $t_{norm} = 2.3$, exhibit rather high values of turbulent kinetic energy, these values increase significantly due to the interaction with the free vortex sheet. This means that the turbulence is significantly augmented by the interaction and the higher fluctuations are eventually advected downstream.

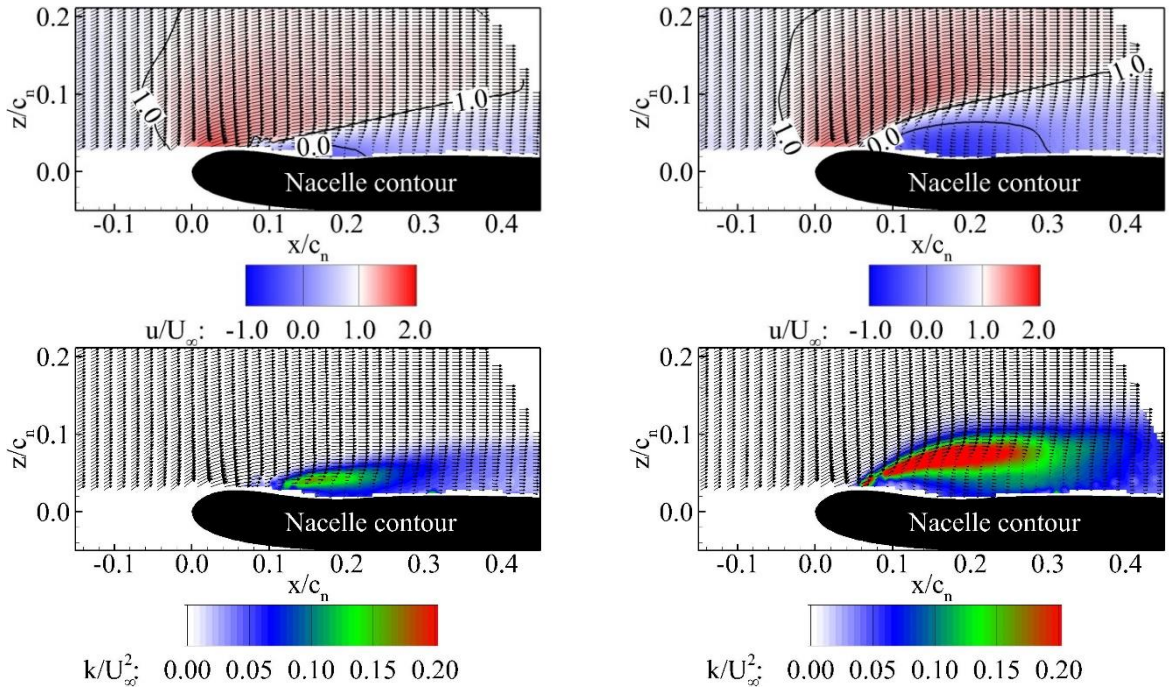

Figure 17. Phase-locked flow field in the symmetry plane of the nacelle at α_n = 21deg. Color mapping of the normalized x-component of the velocity u (above) and for the normalized turbulent kinetic energy (below) for the undisturbed flow at t_{norm} = 2.3 (left) and the disturbed flow t_{norm} = 4.0 (right).

B. Validation Studies on a High-Lift Wing Section

The second experiment represents the effects of disturbed inflow on high-lift airfoil stall, and this was conducted in the low-speed wind tunnel of the TU Braunschweig. A step-by-step approach was followed that began with the study of quasi two-dimensional vortex gusts, followed by more complex, three-dimensional disturbances in vertical and spanwise direction. The experiments were accompanied by corresponding numerical simulations to gain understanding of the complex interactions between the inflow disturbances and the aerodynamics of a two-element airfoil in high-lift configuration. An overview of the setup is given in Fig. 18. It uses two separate wings to serve as disturbance/vortex generators (VG1 and VG2) whereas the two-element high-lift airfoil is located downstream. Either VG1, VG2 or both vortex generators can be placed in the test-section to generate the desired disturbances.

The quasi 2D vortical gust is generated by VG1, using the dynamically rotated NACA 0021 wing section (c=0.3m) as described above. Three-dimensional and spanwise disturbances are induced by VG2. This vortex generator is placed between VG1 and the two-element high-lift airfoil, according to Fig. 18. VG2 is designed as a finite wing based on a NACA 4412 airfoil (c=0.3m). Its angle of attack is adjusted to 2.5 deg, thus creating a longitudinal wingtip vortex. This longitudinal vortex causes two main flow effects. Firstly, it induces a spanwise, steady disturbance at the high-lift airfoil of the same order as the vertical gust of VG1. Furthermore, if VG2 is used along with VG1, the 2D gust of VG1 is distorted three-dimensionally. With this modular experiment, various disturbance cases of increasing complexity can be realized: 1.) Quasi 2D, transient disturbances by VG1, 2.) 3D, but steady disturbances by VG2, and 3.) 3D and transient disturbances by VG1 and VG2 together.

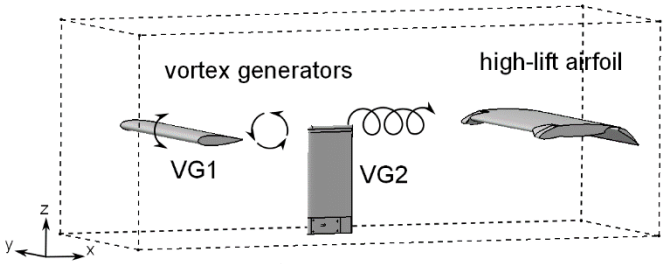

Figure 18. Sketch of the wind tunnel/simulation setup

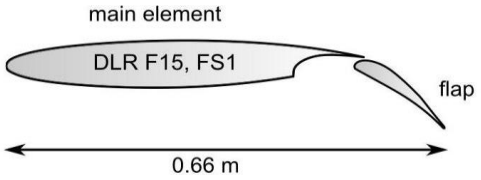

Figure 19. DLR-F15 high-lift airfoil

These disturbances distort the flow around the high-lift airfoil. This two-element configuration is based on the DLR-F15 airfoil[33] (c=0.6m for clean airfoil), see Fig. 18. The leading edge of the main element is located 2m downstream of trailing edge of VG1 in its zero deg position and 1m downstream of the trailing edge of VG2. Various measurement techniques are used in the experiment to obtain insight into the flow around the airfoil and its aerodynamic behavior and to provide a validation database for numerical simulations. Among these techniques are time-averaged and time-resolved surface pressure measurements, steady and phase-locked stereoscopic particle image velocimetry (S-PIV), flow measurements with a time-resolving five-hole-probe, as well as qualitative investigations by oiflow and tuft visualizations. The distributions of the time-resolved surface pressure was experimentally recorded by means of numerous fast-response pressure sensors close to the airfoil's mid-section. Data accumulate over more than 80 pitch cycles of VG1, providing ensemble averages. The measurements were performed at various angles of attack in the linear lift regime, around maximum lift conditions and at stall. Three different angles of attack are selected for comparisons with simulations, i.e. 0, 6 and 9 deg. At zero degree, the flow separates partly from the flap, while the flow over the main element is attached. Increasing the angle of attack reduces the size of the separation on the flap, so that at 6deg the flow over main element and flap is attached. A further increase of the angle of attack leads to incipient separation near the main element trailing edge. At 9deg the airfoil is beyond its maximum lift coefficient and close to stall.

The numerical simulations use hybrid grids with the entire vortex transport taking place in a structured grid area. The grid for two-dimensional computations consists of about 360.000 points, whereas the 3-dimensional grid utilizes 16.4×10^6 points. For reducing the numerical effort, the tunnel wall boundary layers are not resolved, instead we assume slip-wall conditions. Note that the numerical onset flow conditions match the reading of a Prandtl probe mounted in the test-section. The Reynolds number is 2×10^6, based on the clean airfoil chord length. The grid of the vortex generator VG2 is embedded using the Chimera technique. For generating the unsteady disturbance in the simulation, the TAU-code represents the pitching motion of VG1 by using the grid deformation method[23]. Initial URANS-simulations used the Menter SST model as well as the JHh-v2 and JHh-v3 models. Both Reynolds stress models showed an oscillating flow behavior in the cove region and in the shear layer above the flap, while these low

frequency oscillations were not observed in the experimental data[34,37]. For this reason, only results of the Menter SST model are displayed in the following.

As mentioned above, three different disturbance cases are designed and presented in the following. First, the 2D transient disturbance by VG1 is discussed, followed by the 3D steady disturbance by VG2. Finally, the 3D transient flow generated by VG1 and VG2 is evaluated.

In the first step the appropriate simulation method for the generation and transport of the model gust of VG1 is investigated[35]. The rapidly deflecting NACA0021 airfoil, which is rotated by 10 deg within 15 ms, is modeled with URANS up to its trailing edge. The vortex characteristics of the gust are advected as part of the airfoil wake. This process is simulated with URANS and ADDES, and the results are compared with the experiments. Regarding the ADDES, we find that at least stochastic forcing of the subgrid eddy viscosity in the wake is necessary in order to obtain three-dimensional turbulent structures. Without forcing the flow maintains a non-physical, two-dimensional character. In Fig. 21 the gust appears as a bend in the wake behind the deflected NACA0021 airfoil using ADDES.

In the simulations as well as in the experiments, time-resolved data are taken in the wake at the location where the DLR-F15 airfoil is eventually positioned. Fig. 21 presents the comparison of the flow incidence angle and the axial velocity induced by the rotation of VG1. The gross effects of the gust are similarly reproduced by RANS and ADDES. Hence, using URANS avoids the significant computational costs for a scale-resolved wake of VG1.

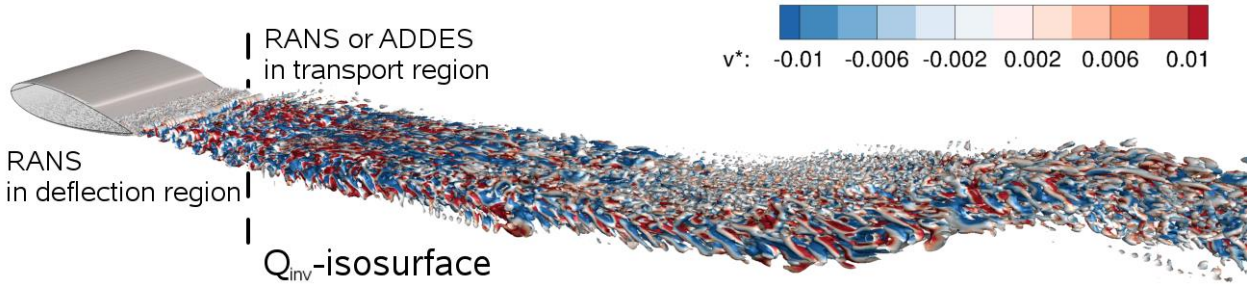

Figure 20. Resolved turbulent structures in the wake of the deflected NACA0021 gust generator airfoil VG1

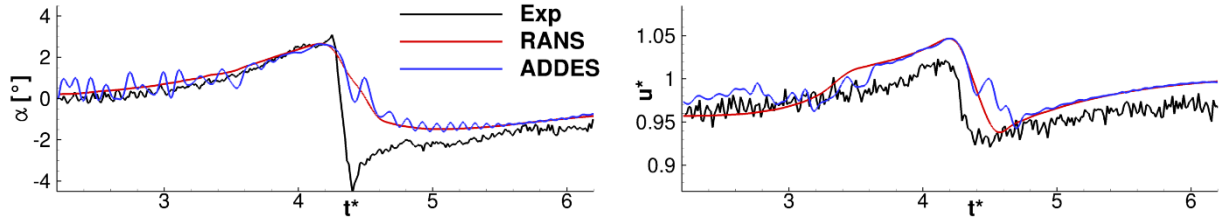

Figure 21. Time sequence of the angle of attach and normalized velocity introduced by VG1

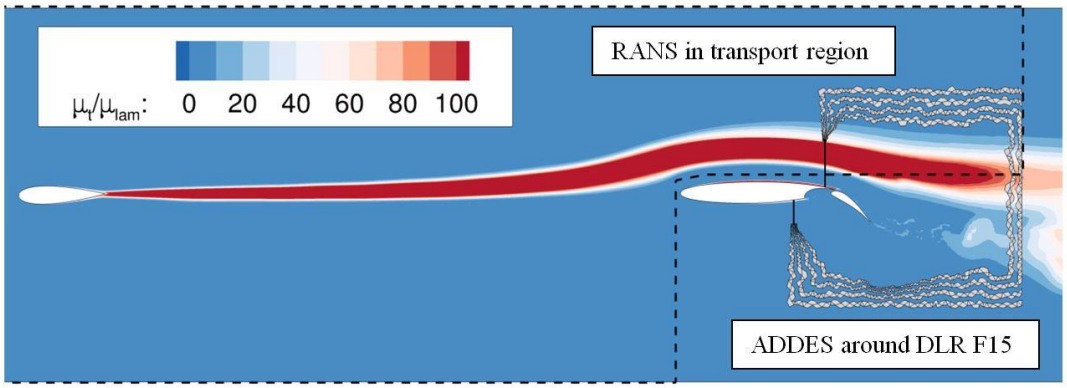

Figure 22. Assignment of RANS/ADDES zones in the simulation setup and computed distribution of the eddy viscosity

These results set the stage for simulating the steady and transient flow field of the DLR-F15 high-lift airfoil and VG1 by using URANS and the hybrid simulation approaches described in Section II. In the present test case, the vortex path is located along the upper side of the DLR-F15 airfoil at zero deg angle of attack. The transport of the gust is simulated in RANS mode while ADDES is used in the region around the DLR F15 airfoil during hybrid simulations, as shown in Fig. 22. The coarser span-wise grid resolution that is sufficient for RANS is refined only in the region around the flap. The transition elements in Fig. 22 indicate the region where the grid is adapted in the span-wise direction. With this approach the number of grid points is considerably reduced, i.e., only 56% of the points of a globally fine grid are needed. In the region above the flap the level of eddy viscosity is strongly reduced compared to RANS allowing the development of resolved turbulence. Fig. 23 displays the turbulent structures by an iso-surface of the Q-criterion. The dark green area on the upper side of the main wing indicates the location, where synthetic turbulent structures are fed into the flow, while the reference values for the turbulence generator are taken from the light green area. The induced structures destabilize the boundary layer on the main wing and lead to a fast break-up of the shear layer downstream of the main-element trailing edge.

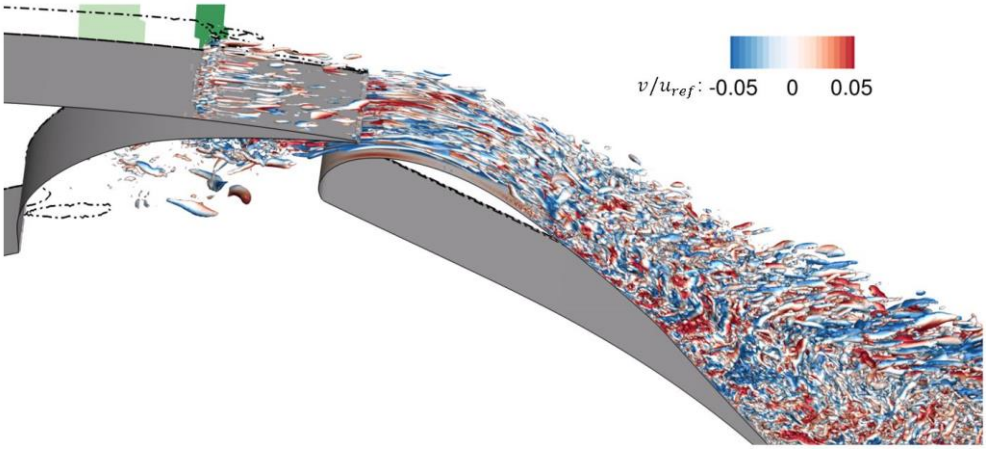

Figure 23. Resolved turbulent structures in the flap region of the 2-Element high-lift airfoil resolved by the ADDES with synthetic turbulent forcing

Fig. 24 shows an ADDES result of the transient VG1 case[35]. Here the mean difference-velocity vectors illustrate the position of the vortex during the interaction with the two-element airfoil. The image sections visualize three different normalized time instants, $t^* = t/t_{ref}$, where t_{ref} is defined using the free-stream velocity of 50.5m/s and the airfoil chord of c=0.6m. At $t^* = 4.25$ the vortex has reached the leading edge of the high-lift airfoil. At $t^* = 4.625$ the vortex stretches in the accelerated flow over the main wing and therefore is less sharply defined. Finally, at $t^* = 5.25$ the vortex has passed the high-lift airfoil. The positions where the vortex core was detected in the experimental investigation[38] are denoted by the yellow symbols, while the the blue line indicates the extrapolated vortex path. As the results confirm, the simulation setup of the high-fidelity method is suited to investigate the airfoil-vortex interaction.

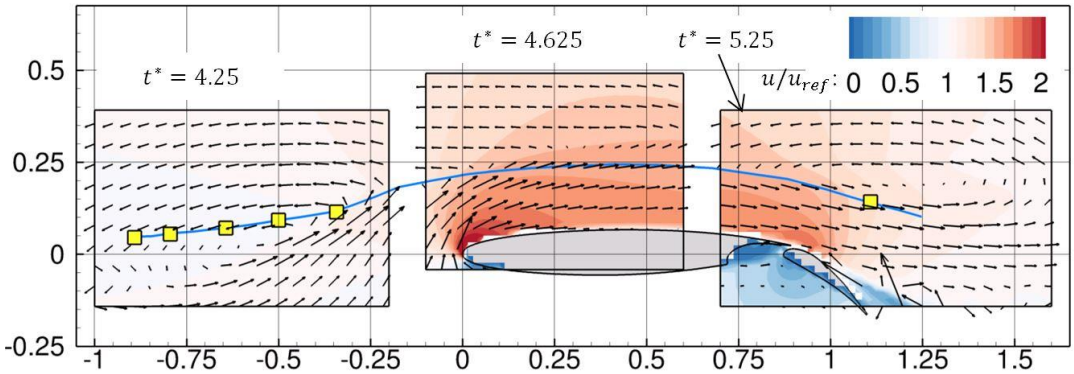

Figure 24. Vortex positions at different time instances during the interaction with the high-lift airfoil

In principle, the method is able to predict the influence of the different scales of the disturbance. Especially the influence of the small-scale disturbances can provide detailed insights into the mechanisms of the interaction. However, in the special setup of the VG1 case, this advantage is not fully exploited, as the vortex passes the high-lift airfoil at a certain distance. Moreover, to investigate varying setups of the vortex generator a computationally less expensive approach is needed.

Our work provided a large number of URANS-computations for the transient VG1 case. Fig. 25 shows the experimental and numerical time traces of the static pressure disturbance, ΔC_P at two chord wise positions. The agreement between simulations and experiment is good. Both the numerical and experimental data reveal very similar sensitivities of the static pressure. They exhibit two main disturbance effects, namely a circulation effect and an induced velocity effect. For all angles of attack investigated, the main-element leading edge is sensitive to the induced flow angles of the vortex. At the time instant of maximum surface pressure disturbance, the core region of the transversal vortex is still upstream of the leading edge, thereby increasing the circulation of the airfoil. In contrast, the induced stream-wise velocity of the passing vortex dominates the disturbance at the rear-part of the main element and the leading edge of the flap. This effect was likewise identified by an evaluation of the flow field in the vicinity of the pressure sensors. Interestingly, the effect of the disturbance varies at the trailing edge of the flap. For low angles of attack, with flow separation on the flap, this region is sensitive to the circulation of the main-element. In contrast, at higher angles of attack with attached flow, this region appears rather dominated by the induced velocity effect. Ref. 38 gives more details.

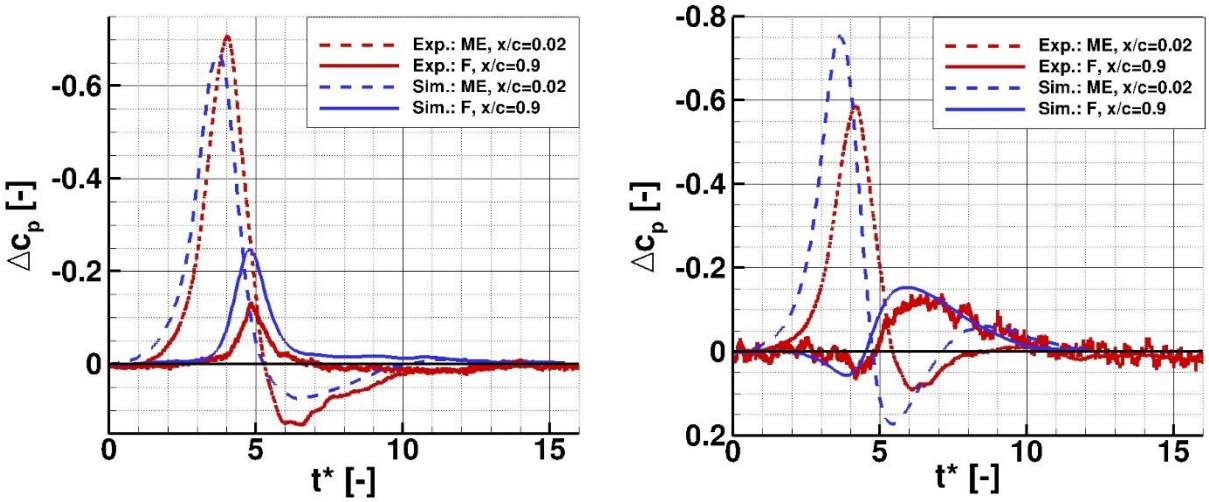

(a) α=0 deg **(b) α=6 deg**

Figure 25. Disturbance of the static surface pressure along the high-lift airfoil during interaction with the 2D, transient gust of VG1.

The 2D disturbance case was further numerically analysed for its sensitivities. Besides the angle of attack of the high-lift airfoil airfoil also the vertical position and the rotation of the gust generator were varied. Changing the position of the gust generator upwards or decreasing the rotation speed caused rather modest effects on the interaction at the high-lift airfoil. Furthermore, most of the sensitivity is restricted to the leading edge of the main element. Differences decrease further downstream, probably due to stretching of the vortex along the upper side of the high-lift configuration. Reversing the vortex rotation resulted in a reversal of the disturbance at the high-lift airfoil, but no new physical effect was observed. A new type of interaction was found for the specific configuration where the vortex impinges at the leading edge of the high-lift airfoil. In that case the vortex splits into a stronger part above and a weaker part below the airfoil[37]. The stronger part moves along the upper side of the airfoil and causes similar reactions as for the basic test case. The weaker part advects along the lower side with much lower velocity towards the cove region, where the distortion remains. Hence, the pressure distribution is influenced for a long period of time. Even six non-dimensional time units after the vortex has reached the cove, the pressure distribution is still disturbed by the presence of this slowly travelling vortex, see Fig. 26.

The steady, three-dimensional disturbance caused by VG2 was also investigated. Since VG1 is part of the more complex transient 3D disturbance case, this airfoil remained in the test-section, and was set at zero incidence. The

wing-tip vortex has two major effects on the flow field. Firstly, the wake of VG1 is three-dimensionally distorted, as seen in Fig. 27. It appears that the wake of VG1 is pushed downwards on the right airfoil side, being now closer to the airfoil surface. On the left side, the wake is shifted upwards. This results in a varying interaction distance between the vortex of VG1 and the high-lift configuration. Secondly, the onset flow to the high-lift configuration becomes three-dimensional. The wingtip vortex of VG2 causes a spanwise variation of induced flow angles, which affects airfoil circulation.

The effect of this variation on the spanwise pressure distribution at the main element leading edge for α=0deg can be seen in Fig. 28. Due to the anti-clockwise rotation of the wingtip vortex, C_P-values are reduced at negative spanwise positions and increased at positive spanwise positions. This likewise affects the extent of the separation region on the flap. The higher circulation associated with lower C_P-values leads to a reduced separation. This is seen in in the separation line (not shown here), and qualitative agreement between the simulation and experiment is obtained. At high angles of attack of the high-lift airfoil, the steady wingtip vortex causes a span-wisely inhomogeneous stall behaviour. Stall begins at the left side of the wing section where the vortex induces effectively higher angles of attack.

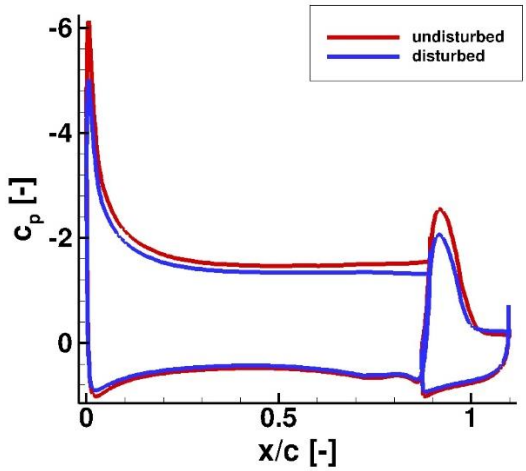

Figure 26. Computed pressure distribution of DLR F15 airfoil at α=0deg, red: before gust interaction, blue: 6 convective time units after the vortex arrived at the cove region.

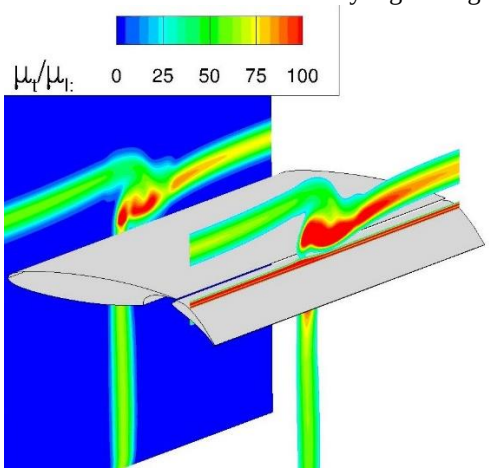

Figure 27. Combination of VG1 wake and VG2 tip vortex interacting with DLR-F15 airfoil at α=0deg, contour plot: ratio eddy viscosity over laminar viscosity at x/c=0 and x/c=0.97

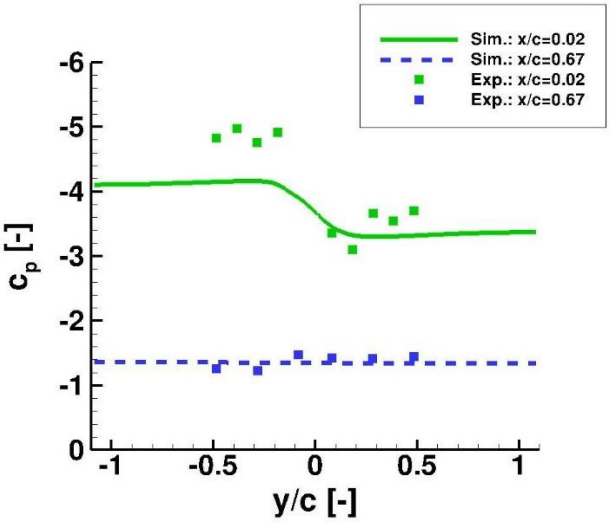

Figure 28. Comparison of pressure coefficient along span for stationary VG1-VG2 case at α=0 deg

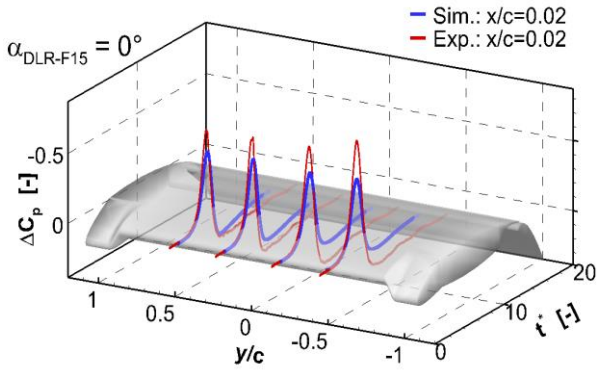

Figure 29. Comparison of pressure coefficient time traces at four spanwise location for unsteady VG1-VG2 transient

On the basis of the results for steady 3D disturbances, transient 3D disturbances are now discussed. Here, the 2D gust of VG1 interacts with the 3D wingtip vortex of VG2. Fig. 29 shows the numerical and experimental time traces at the location of four fast-response pressure sensors on the main element leading edge for zero degree angle of attack. Again, data were acquired for more than 80 pitch cycles of VG1 and ensemble averaged afterwards. For reasons of clarity, the distortion of pressure, $\Delta C_{P,}$ based on the steady C_P-values in Fig. 27 is shown. The DLR-F15 airfoil is depicted in the background to visualize the span-wise location of the pressure sensors. The time traces of the simulations and the experiments agree rather well. Small differences occur around $\Delta C_{P,min}$ and after the gust has passed the airfoil. The experimental data reveal slightly lower C_P-values for negative spanwise positions, whereas no such effect is visible in the simulation results. Note that this is the region, where both gust and wingtip vortex induced higher angles of attack.

VI. Conclusion

The present paper describes cooperative works of the DFG Research Unit 1066 to simulate wing and nacelle stall of generic transport aircraft geometries. The research aims at including the effects of gusts that distort the onset flow. Therefore, fundamental research addresses turbulence modeling, atmospheric gust modeling, suited computational approaches, validation experiments and corresponding validation simulations. The paper serves to disseminate the results to the international audience. The obtained data on stall phenomena is publically open and can be shared with other research groups who seek cooperation on the subject.

Acknowledgments

The authors gratefully acknowledge the funding of Research Unit 1066 by the Deutsche Forschungsgemeinschaft, DFG.

References

[1] www.for1066.de , December 2015.

[2] Niehuis, R.; Lesser, A.; Probst, A.; Radespiel, R.; Schulze, S.; Kähler, C.; Spiering, F.; Wartzek, F, Schiffer, H.-P., "Simulation of Nacelle Stall and Engine Response". *21th ISABE Conference*, 9-13 September 2013, Busan, Korea, 2013.

[3] Radespiel, R.; Francois, D. G., Hoppmann, D., Klein, S., Scholz, P., Wawrzinek, K., Lutz, T., Auerswald,T. , Bange, J., Knigge, C., Raasch, S., Kelleners, P., Heinrich, R., Reuß, S., Probst, A., Knopp, T.: Simulation of Wing Stall, AIAA-2013-3175, 2013.

[4] Schwamborn D., Gerhold T., Heinrich, R.: The DLR TAU-Code: Recent Applications in Research and Industry. In Proceedings of European Conference on Computional Fluid Dynamics ECCOMAS CDF 2006, Egmond aan Zee, The Netherland, 2006.

[5] Cécora, R.-D., Eisfeld, B., Radespiel, R., Probst, A.: "Differential Reynolds Stress Modeling for Aeronautics". .: Differential Reynolds-Stress Modeling for Aeronautics, AIAA Journal, Vol. 53, No. 3, 2015, pp.739-755.

[6] Cécora R., Radespiel R., Jakirlic S.: Modeling of Reynolds-stress augmentation in shear layers with strongly curved velocity profiles. The world congress on computational mechanics, 11th World Congress on Computational Mechanics (WCCM XI), 5th European Conference on Computational Mechanics (ECCM V), 6th European Conference on Computational Fluid Dynamics (ECFD VI), Barcelona, Spain, 2014.

[7] Jakirlic, S., Hanjalic, K., "A new approach to modelling near-wall turbulence energy and stress dissipation". *Journal of Fluid Mechanics*, Vol. 459, No 1, Cambridge Univ Press., 2002, pp. 139-166.

[8] Probst, A., Radespiel, R., Rist, U., "Linear-Stability-Based Transition Modeling for Aerodynamic Flow Simulations with a Near-Wall Reynolds-Stress Model". *AIAA Journal*, Vol. 50, No 2, American Institute of Aeronautics and Astronautics, 2012, pp. 416-428.

[9] Menter, F. R.: "Two-Equation Eddy-Viscosity Turbulence Models for Engineering Applications". AIAA Journal, Vol. 32, No. 8, August 1994, pp. 1598-1605.

[10] Knopp, T., Probst, A., "An Algebraic Sensor for the RANS-LES Switch in Delayed Detached-Eddy Simulation". New Results in Numerical and Experimental Fluid Mechanics VIII. Notes on Numerical Fluid Mechanics and Multidisciplinary Design, Volume 121, 2013, pp. 457-464.

[11] Probst, A., Radespiel, R., Knopp, T., "Detached-Eddy Simulation of Aerodynamic Flows Using a Reynolds-Stress Background Model and Algebraic RANS / LES Sensors". AIAA-2011-3206, 2011.

[12] Adamian, D., Travin, A.: "An Efficient Generator of Synthetic Turbulence at RANS-LES Interface in Embedded LES of Wall-Bounded and Free Shear Flows". In Computational Fluid Dynamics 2010, Russia, Springer, pp. 739-744, (2011).

[13] François, D. G., Radespiel, R., Probst, A.: "Airfoil Stall Simulations with Algebraic Delayed DES and Physically Based Synthetic Turbulence for RANS-LES Transition". AIAA-2014-2574, (2014).

[14] François, D. G., Radespiel, R., Reuss, S., Probst, A.: Computation of Separated Flows with a Hybrid RANS/LES Approach. Symposium "Simulation of Wing and Nacelle Stall". 1-2 Dec 2014, Braunschweig, Germany. In: Notes on Numerical Fluid Mechanics and Multidisciplinary Design, Vol. 131, Springer-Verlag, 2015.

[15] François, D. G., Radespiel, R., Probst, A.: Forced synthetic turbulence approach to stimulate resolved turbulence generation in embedded LES. Published in Hybrid RANS-LES Modelling, doi: 10.1007/978-3-319-15141-0_ 6, 2014.

[16] Probst, A. and Reuß, S.: Scale-Resolving Simulations of Wall-Bounded Flows with an Unstructured Compressible Flow Solver. Progress in Hybrid RAN/LES Modelling, Notes on Numerical Fluid Mechanics and Multidisciplinary Design. Vol. 130 pp. 93-103, Springer International Publishing, 2015.

[17] Probst, A., Schulze, S., Kähler, C. J., Radespiel, R.:Numerical Simulation of Engine-Inlet Stall with Advanced Physical Modelling Compared to Validation Experiments. In: Notes on Numerical Fluid Mechanics and Multidisciplinary Design New Results in Numerical experimental Fluid Mechanics VIII, Vol. 121. pp. 565-573, 2013.

[18] Maronga, B., Gryschka, M., Heinze, R., Hoffmann, F., Kanani-Sühring, F., Keck, M., Ketelsen, K., Letzel, M. O., Sühring, M., and S. Raasch: "The Parallelized Large-Eddy Simulation Model (PALM) version 4.0 for Atmospheric and Oceanic Flows: Model Formulation, Recent Developments, and Future Perspectives", Geosci. Model Dev. Discuss., 8, 1539-1637, DOI: 10.5194/gmdd-8-1539-20, 2015.

[19] Letzel, M.O., C. Helmke, E. Ng, X. An, A. Lai and S. Raasch: "LES case study on pedestrian level ventilation in two neighbourhoods in Hong Kong", Meteorol. Z., 21, 575-589, DOI: 10.1127/0941-2948/2012/0356, 2012.

[20] Knigge, C., Raasch, S.: "Development and Improvement of Two Methods of Different Complexity to Simulate Atmospheric Boundary Layer Turbulence for Aircraft Design Studies". Symposium "Simulation of Wing and Nacelle Stall". 1-2 Dec 2014, Braunschweig, Germany. In: Notes on Numerical Fluid Mechanics and Multidisciplinary Design, Vol. 131, Springer-Verlag, 2015.

[21] Knigge, C., Auerswald, T., Raasch, S. and Bange, J.: "Comparison of two methods simulating highly resolved atmospheric turbulence data for study of stall effects". Computers & Fluids, 108, 2015, pp. 57–66.

[22] Nieuwpoort, A.M.H., Gooden, J.H.M. and de Prins, J.L.: "Wind criteria due to obstacles at and around airports", NLR-CR-2006-261, National Aerospace Laboratory, 2006.

[23] Heinrich, R., Reimer, L. Michler, A., "Multidisciplinary simulation of maneuvering aircraft interacting with atmospheric effects using the DLR TAU code". RTO AVT-189 Specialists' Meeting on Assessment of Stability and Control Prediction Methods for Air and Sea Vehicles, 12.-14. Oktober 2011, Portsdown West, UK.

[24] Kelleners, P., Heinrich, R., "Simulation of Interaction of Aircraft with Gust and Resolved LES-Simulated Atmospheric Turbulence". Symposium "Simulation of Wing and Nacelle Stall". 1-2 Dec 2014, Braunschweig, Germany. In: Notes on Numerical Fluid Mechanics and Multidisciplinary Design, Vol. 131, Springer-Verlag, 2015.

[25] Chesshire, G., Henshaw, W. D., "Composite Overlapping Meshes for the Solution of Partial Differential Equations". Journal of Comp. Physics 90, pp.1-64, 1990.

[26] Kelleners, P., Spiering, F., "CTAU, A Cartesian Grid Method for Accurate Simulation of Compressible Flows with Convected Vortices". Dillman et al. (eds.), New Results in Numerical and Experimental Fluid Mechanics IX, Notes on Numerical Fluid Mechanics and Multidisciplinary Design. Vol. 124, Springer International Publishing Switzerland , 2014.

[27] Enk, S., "Zellzentriertes Padeverfahren für DNS und LES". DLR FB 2015-24, 2015.

[28] Lele, S. K., "Compact Finite Difference Schemes with Spectral-like Resolution". Journal of Comp. Physics 103, pp.16-42 1992.

[29] Hahn D., Scholz P., Radespiel R., "Vortex generation in a low speed wind tunnel and vortex interactions with a high-lift airfoil" AIAA-2012-3024, *30th AIAA Applied Aerodynamics Conference*, New Orleans, Louisiana, June 25-28, 2012.

[30] Übelacker, S., Hain, R., Kähler, C. J. "Flow Investigations in a Stalling Nacelle Inlet Under Disturbed Inflow," 4th Symposium 'Simulation of Wing and Nacelle Stall', Braunschweig, Germany, December 1-2, 2014.

[31] Schulze, S., "Experimentelle Untersuchungen zur Wirbeldynamik am überziehenden Triebwerkseinlauf," Ph.D. Dissertation, Universität der Bundeswehr München., Munich, Germany, 2012.

[32] Vollmers, H., "Detection of vortices and quantitative evaluation of their main parameters from experimental velocity data," Meas. Sci. Technol., Vol. 12, 2001, pp. 1199-1207.

[33] Wild, J., "Mach and Reynolds Number Dependencies of the Stall Behavior of High-Lift Wing-Sections", J. Aircraft, Vol. 50, 2013, pp. 1202-1216.

[34] Reuß S., Probst A., Knopp T.: Numerical investigation of the DLR F15 two-element airfoil using a Reynolds stress model. Third Symposium Simulation of Wing and Nacelle Stall, Germany, Braunschweig, 21-22 June 2012.

[35] Reuß S., Probst A., Knopp T., Wawrzinek K.: Hybrid RANS/LES Study of the Development of an Airfoil-Generated Vortex. Symposium "Simulation of Wing and Nacelle Stall". 1-2 Dec 2014, Braunschweig, Germany. In: Notes on Numerical Fluid Mechanics and Multidisciplinary Design, Vol. 131, Springer-Verlag, 2015

[36] Reuß S.: A Grid-Adaptive Algebraic Hybrid RANS/LES Method, PhD Thesis, 2015.

[37] Wawrzinek K., Lutz T., Krämer E.: Numerical Studies of Turbulent Flow Influence on a Two-Element Airfoil. Symposium "Simulation of Wing and Nacelle Stall". 1-2 Dec 2014, Braunschweig, Germany. In: Notes on Numerical Fluid Mechanics and Multidisciplinary Design, Vol. 131, Springer-Verlag, 2015.

[38] Klein, S., Hoppmann, D., Scholz, P., Radespiel, R., ``High-lift airfoil interacting with a vortical disturbance: wind-tunnel measurements," AIAA Journal, DOI: 10.254/1.J053441, 2014.